npj | clean water

www.nature.com/npjcleanwater

ARTICLE OPEN

Check for updates

Pyridinic N anchored Ag and Au hybrids for detoxification of organic pollutants

Naveen Kumar Reddy Bogireddy[1]✉, Abdel Ghafour El Hachimi[2], Yetzin Rodriguez Mejia[3], Mohan Kumar Kesarla[4], Rajender S. Varma[5], Raul Herrera Becerra[1] and Vivechana Agarwal[6]✉

The development of a highly reusable, non-toxic catalyst for the effective removal of 4-nitrophenol (4-NP) from marine water is a key challenge due to its diverse effects on living organisms. Herein, in situ green fabricated pyridinic N anchored Ag_2O/Au decorated porous silica (CG-Ag_2O/Au-SiO_2) using spent coffee grounds (CG) powder is introduced as a reusable catalyst to mitigate 4-NP, Methylene blue (MB), Rhodamine 6G (R6G) and their mixture in the spiked deionized, river and marine water samples. Exceptionally high structural activity and excellent reusability of catalysts up to 15 cycles have been demonstrated due to the accessibility of a large number of active sites from pyridinic N-anchored Ag_2O and Au particle surfaces. CG-Ag_2O/Au-SiO_2 with the lower Ag and Au contents of 0.59 and 0.11 wt% (ICP-MS) of active catalytic sites exhibit a superior activity parameter of 6000 s^{-1} g^{-1} (4-NP), 6357 s^{-1} g^{-1} (MB), and 2892 s^{-1} g^{-1} (R6G) than chemically synthesized and reported, bare and hybrid structures. Furthermore, the CG-Ag_2O/Au-SiO_2 shows excellent stability in marine water with promising reusability performance (≈93% after 15 successive cycles). Density functional theory (DFT) studies reveal that the observed high catalytic efficiency originates from the pyridinic N presence on the Ag_2O/Au structures.

npj Clean Water (2022)5:40 ; https://doi.org/10.1038/s41545-022-00187-w

INTRODUCTION

4-Nitrophenol (4-NP) is one of the highly toxic organic pollutants among the substances bearing nitro group[1–5]. It is recognized as a priority hazardous pollutant by the Environmental Protection Agency (EPA) due to its poisonous and volatile nature[1,4,6,7]. 4-NP is used in several industries, namely the manufacturing of drugs (e.g., acetaminophen), pesticides (e.g., ethyl and methyl parathion), pH indicators, and dyes[6,8]. 4-NP enters into the aqueous environment by the accumulation of waste products from numerous industries. Importantly, 4-NP is an intermediate product in acetaminophen (paracetamol) production via a three-step procedure from phenol and converts acetylate amino group to paracetamol. Furthermore, 4-NP is a severe threat to human health due to direct exposer via drinking contaminated water and occupational exposure for the workers in the 4-NP production or industries utilizing it[8]. Exposure to 4-NP may affect nervous systems and brain damage in the human body[6]. Due to its high stability and solubility in an aqueous environment, it can be identified in two common forms in an aqueous medium, 4-NP (at pH < 6.5), and it is common ionic (at pH > 6.5) form, which can easily be distinguished by naked eye with visual change in the color from pale yellow ($\lambda_{max} \approx 317$ nm) to dark yellow ($\lambda_{max} \approx 400$ nm) ionic transformation[6]. There are several approaches available for the removal of 4-NP from aqueous solution[8–10]. Among them, $NaBH_4$-based probe reaction gained more attention[5] due to its highly efficient and rapid reduction process and the superb use of the ensued reduced product, 4-aminophenol (4-AP) in pharmaceutical industries. Thus, fabricating a highly efficient and reusable catalyst to remove 4-NP including other textile organic dyes such as methylene blue and rhodamine 6G from marine water is a significant priority task[11–18].

Traditional bare metal nanoparticles and their composite catalysts, e.g., Ag–NP/C spheres, TAC–Ag, Ag/SiNSs, Ag/C, Ag/SNTs, CNFs/Ag, Fe_3O_4@SiO_2–Ag, Ag@SBA, Ag/KCC-1, and Ag_2O/Au-DMSNs[19–27]. Furthermore, among the four types of nitrogen atom (pyridinic N, pyrrolic N, graphitic N, and amine N) bearing catalysts, pyridinic nitrogen atoms are known for their efficiency to improve the activity of carbon-based catalysts in catalytic reduction reactions[28–31]. Usually suffer from lack of removal efficiency and poor stability towards reusability; design and development of green fabricated metal hybrid structures with abundant active sites may address the mentioned problems[8,11]. Specifically, noble metal-based composites have garnered more interest as they exhibit high catalytic efficiency towards reducing 4-NP[2,4,32,33] wherein generally increasing the metal content and decreasing the particle size of the catalyst is considered vital to increase 4-NP removal effectiveness. Dong et al.[20] reported the outstanding activity parameters for Ag NPs (8.97%) decorated fibrous nano-silica (50 s^{-1} g^{-1}) for the reduction of 4-NP. Later, Yang et al.[25] obtained excellent activity strictures (90 s^{-1} g^{-1}) using Au/Ag_2O dispersed onto dendritic mesoporous silica nanospheres with metal contents of 1.0% each. Since metal nanoparticle surfaces are the possible reactive species, altering the fabrication technique, concentration of metal content, and facet of the nanoparticles onto the support would significantly improve the catalytic efficiency; there is a paucity of such hybrid structure for the removal of 4-NP using $NaBH_4$.

[1]Instituto of Physics, National Autonomous University of Mexico (UNAM), P.C. 04510 Mexico, Mexico. [2]Centro de Investigaciones Químicas, Universidad Autónoma Del Estado de Morelos, 62210 Cuernavaca, Morelos, Mexico. [3]Faculty of Chemistry, Autonomous University of the State of Mexico, Paseo Colón-Paseo Tollocan s/n, P.C. 50120 Toluca, Mexico state, Mexico. [4]Institute of Physical Sciences, National Autonomous University of Mexico, P.C. 62210 Cuernavaca, Morelos, Mexico. [5]Regional Centre of Advanced Technologies and Materials, Czech Advanced Technology and Research Institute, Palacky University in Olomouc, Slechtitelu 27, 783 71 Olomouc, Czech Republic. [6]Research Center in Engineering and Applied Sciences, Autonomous University of the State of Morelos (UAEM), Univ. Av. 1001, Col. Chamilpa, 62209 Cuernavaca, Morelos, Mexico.
✉email: naveenbogireddy@fisica.unam.mx; vagarwal@uaem.mx

Silver (Ag) decorated silica-based composites are one of the most common hybrid structures reported for enhanced antimicrobial activity[34], sensors[35], photocatalysis[25], and reduction 4-NP[36] due to their superb attributes such as ease of amine-functionalization, high surface area, and thermal stability. However, there is no report on using in-situ green fabrication exploiting an abundant amount of used ground coffee waste as support (CG-Ag_2O/Au-SiO_2) for the 4-NP reduction in marine water. Catalysts with low content (from XPS) of Ag (5.17 at%) and Au (0.83 at%) are used as efficient, highly reusable hybrid structures to reduce 4-NP in distilled, river, and marine water spiked samples. The green fabricated hybrid structure containing pyridinic N anchored CG-Ag_2O/Au-SiO_2 exhibited an excellent optimized 4-NP, MB, and R6G activity parameter of 6000, 6357, and 2892 s^{-1} g^{-1} outpacing reported Ag-based catalysts[25]; superior kinetics of 4-NP reduction (220 s) was exhibited in marine water, which is quicker than reactions performed in distilled water which bodes well for the efficient removal of 4-NP from marine water. Additionally, the CG-Ag_2O/Au-SiO_2 can be easily recycled up to 15 times with a negligible loss in the 4-NP removal efficacy (≈7%).

RESULTS AND DISCUSSION

The solutions of $AgNO_3$ and $HAuCl_4$ with amine-functionalized SiO_2 were incubated when Ag^+/Au^{3+}-SiO_2 formation can be observed. When this complex is treated with the strong reducing agent $NaBH_4$, it formed Ag/Au-SiO_2 composite where Ag^+ and Au^{3+} both ions were completely reduced (Ag^0/Au^0). However, when the same complex was treated with CG extract or Na-Citrate (mild reducing agent) at 60 ± 5 °C, we observed the formation of Ag_2O/Au-SiO_2 in which only Au^{3+} and Ag^+ were reduced to pure Au metal (Au^0) and Ag_2O nanoparticles. Their formation was confirmed via observations derived from the following characterizations.

The crystallinity and phase structure of the fabricated hybrid structures were recorded using an X-ray diffraction study as presented in Fig. 1, which reveals the hybrid structures comprising two distinct phases, Ag/Au-SiO_2 and Ag_2O/Au-SiO_2. The hybrids fabricated at ambient temperature using $NaBH_4$ alone and $NaBH_4$ with β-CD exhibit the formation of Ag/Au-SiO_2 and it is in good agreement with the JCPDS No. 04-0783[37]. The diffraction peaks at $2\theta \approx 38.4$, 44.5, 64.7, 77.6, and 81.7 can be assigned to (111), (200), (220), (311), and (222) reflections of the face-centered cubic (FCC) structure of Ag or Au structure, which confirms the complete reduction of Ag^+ and Au^{3+} to their nano form (Ag^0 and Au^0). Further, the XRD patterns of the hybrids fabricated using CG extract and CIT at 60 °C show the formation of Ag_2O/Au-SiO_2 structures. The revealed diffraction peaks at $2\theta \approx 32.6$, 46.5, 55.2, 74.9, and 77.0 correspond to Bragg reflections (110), (200), (220), (311), and (222), respectively. The attained XRD patterns clearly show the formation of Ag_2O, which closely matches with commercial Ag_2O spectra JCPDS No. 01-076-1393[38]. The sharp peaks suggest that the formed Ag_2O structures are highly crystalline. Moreover, the presence of a small broad Au (111) was also identified in the hybrids fabricated using CG extract and CIT, which suggests the obtained hybrid has a low percentage of Au and the complete formation of Ag_2O without impurities or other phases (i.e., Ag_2O) in the Ag_2O/Au-SiO_2 hybrids.

Figure 2 shows typical transmission electron microscopy (TEM) images of the fabricated CG-Ag_2O/Au-SiO_2 hybrids. Figure 2a reveals the successful in-situ formation of Ag_2O/Au (*ca.* 20 ± 5 nm for Ag_2O and 3.4 ± 1.6 nm for Au NPs, *d*-values 0.27/0.23 nm) nanoparticles onto SiO_2 substrate, which closely match with the crystallite sizes 4.428 and 22.06 nm for Au (111) and Ag_2O (110) NPs calculated by using Scherrer's equation ($D = \frac{k\lambda}{\beta cos\theta}$) from the obtained XRD patterns, where *D* is crystallites size in nm, *k* is Scherrer constant (0.9), λ is X-ray source wavelength (0.15406 nm),

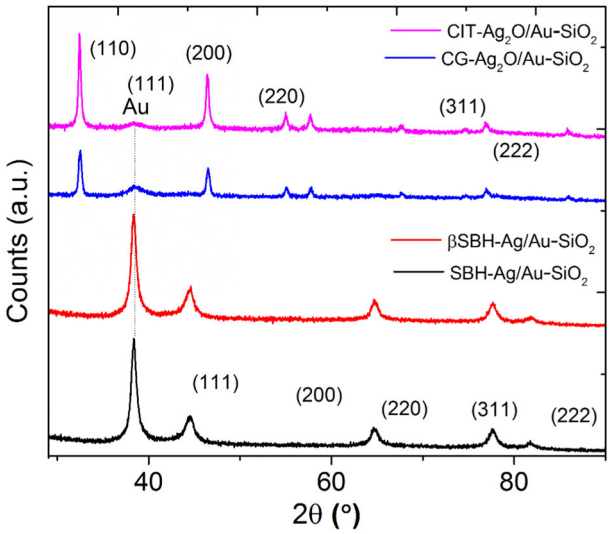

Fig. 1 XRD patterns of hybrid structures. XRD patterns of hybrid structures fabricated using $NaBH_4$ (black), $NaBH_4$ + β CD (red), CG extract (blue), and sodium citrate (pink).

β is full-width half maxima (radians) and θ is peak position (radians).

The high-resolution image exhibits the presence of smaller particles (AuNPs) on the bigger-sized (Ag_2O NPs) particles with distinct interplanar distances, which further affirms the formation of bigger highly crystalline Ag_2O particles with the smaller AuNPs. Figure 2f–l and Supplementary Fig. 1 depict the image mapping and line mapping on Ag_2O/Au NPs, which confirms the presence of both Ag and Au in a single particle. The EDX results contain a higher concentration of Ag (67.8%) compared to Au (32.2%) alone, without measuring the other species present in the hybrid structures. The contribution of the high Ag content and crystallinity closely matches with the obtained XRD patterns intensities. The formation of bigger Ag_2O nanoparticles was identified in the case of CIT-mediated hybrid structures possibly due to the lack of availability of active reducing sites in the CIT (Supplementary Fig. 2).

The elemental composition/chemical oxidation states of fabricated CG-Ag_2O/Au-SiO_2 and CIT-Ag_2O/Au-SiO_2 hybrids were identified using XPS studies. The Ag 3*d* spectrum for Ag species exhibited two distinct peaks due to the presence of Ag $3d_{5/2}$ and Ag $3d_{3/2}$ transitions shown in Fig. 3a, b. The $3d_{5/2}$ peak of single Ag species was deconvoluted into two components at 367.3, and 368.6 eV were assigned to Ag^+ (Ag (I), red) and Ag (Ag (0), green), respectively, and the high content of Ag (I) (≈86%) compared to Ag (0) (≈14%) also noticed[25].

The Au 4*f* spectra exhibited two major species due to Au $4f_{7/2}$ and Au $4f_{5/2}$ transitions (Fig. 3c, d). The Au $4f_{7/2}$ peak of CG-Ag_2O/Au-SiO_2 hybrids further deconvoluted into 83.2 and 84.4 eV peaks which were assigned to Au^0 and $Au^{\delta+}$ (intermediate), respectively[25]. The absence of Au_2O_3 (≈84.0 eV) was noticed, confirming the formation of pure Au nanoparticles. Similar to Ag 3*d* of CG-Ag_2O/Au-SiO_2 hybrids, CIT-Ag_2O/Au-SiO_2 hybrids also observed a more intense and higher energy shift of Au 4*f* due to more than two folds higher content of Au (1.79 at%) than CG-Ag_2O/Au-SiO_2 hybrids Au (0.83 at%) content.

The N 1*s* spectra of CG-Ag_2O/Au-SiO_2 hybrids were mainly deconvoluted into two peaks 399.5 and 401.2 eV assigned to pyridinic N and amine N (Fig. 3e). There is almost negligible N 1*s* spectra intensity is observed in CIT-Ag_2O/Au-SiO_2 hybrids[6]. It is worth noticing that the N 1*s* that appeared in CG-Ag_2O/Au-SiO_2 are due to the presence of nitrogen-containing compounds in the CG, such as caffeine, trigonelline, and other proteins[39]. Especially, the

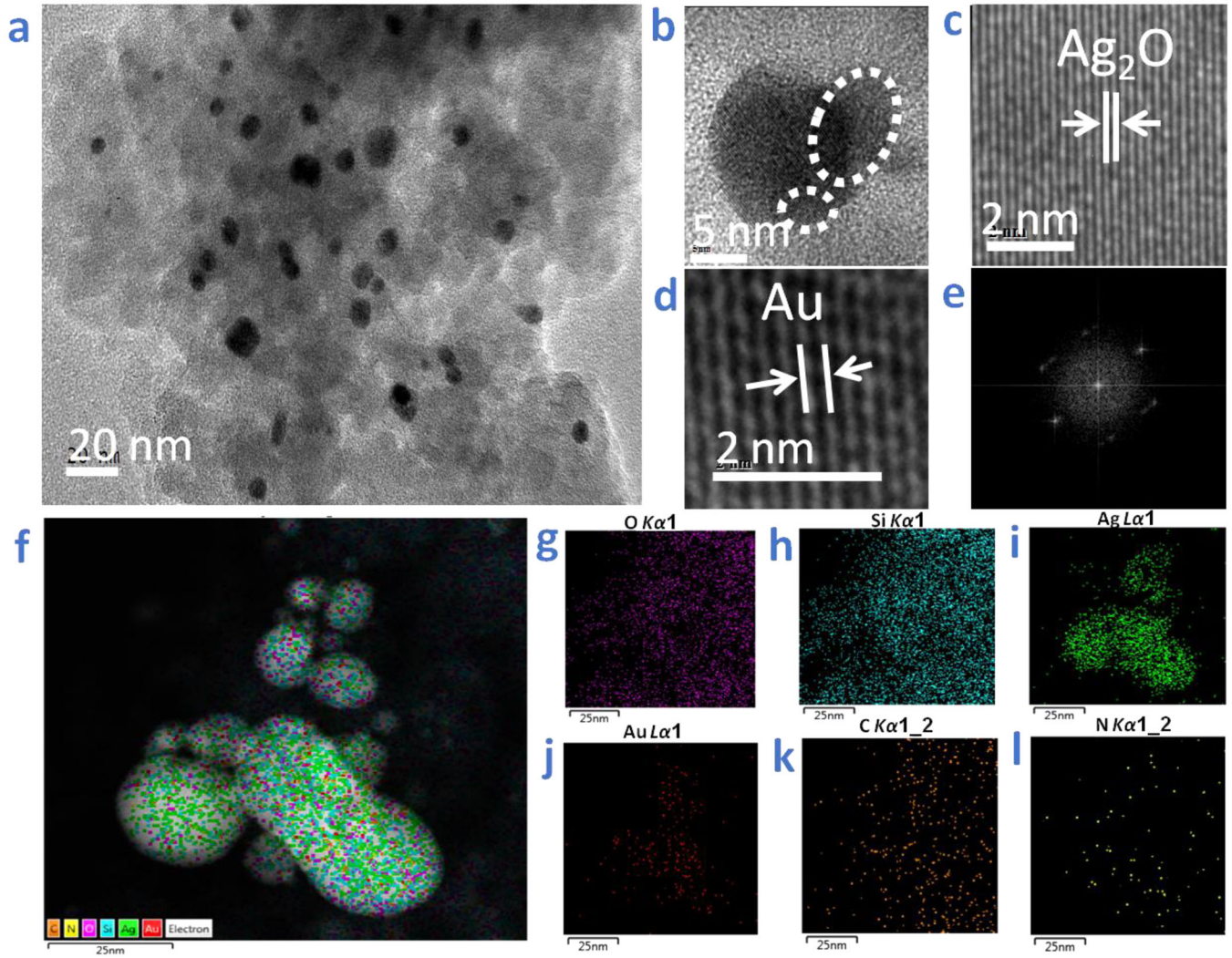

Fig. 2 HR-TEM, FFT, and the EDS mapping of CG–Ag_2O/Au–SiO_2. **a** TEM (scale bar_20 nm), **b**–**d** HR-TEM (scale bars_2–5 nm), **e** FFT, and **f** the EDS mapping of CG-Ag_2O/Au-SiO_2 (scale bars_25 nm) revealing the presence of **g** Oxygen (O (*Kα*1)), **h** Silicon (Si (*Kα*1)), **i** Silver (Ag (*Lα*1)), **j** Gold (Au (*Lα*1)), **k** Carbon (*Kα*1_2), and **l** Nitrogen (*Kα*1_2).

peak at 401.2 eV is generated presumably due to the anchoring of pyridinic N via electrostatic interaction between COO^- groups of trigonelline (a pyridine derivative) and Au/Ag_2O surfaces. The existence of low-intensity amine N confirms the presence of functionalized amine (NH_2) groups on the surface of SiO_2.

Further, the existence of higher content of carbon in the CG-Ag_2O/Au-SiO_2 (39.2 at %) than in CIT-Ag_2O/Au-SiO_2 (22.9 at%) hybrids and the negligible intensities of C=O (287.1 eV) and O–C=O (288.6 eV) species identified in the CIT-Ag_2O/Au-SiO_2 than CG-Ag_2O/Au-SiO_2 structures authenticates the presence of biomass species in the fabricated structures (Supplementary Fig. 3).

A significant, lower energy shift of SiO_2 (103.3 eV) is observed in CG-Ag_2O/Au-SiO_2 hybrids due to the electron transfer between the Au NPs and Pyridinic N (Fig. 3f)[19].

Above mentioned analytical methods (TEM and XPS) are well-established protocols often used to characterize nanoparticles. Additionally, the determination of the concentration of the Ag and Au on the surface of the silica support was also carried out by solution-mode ICP-MS. The concentrations provided by the other methods (TEM and XPS) are several times higher than the concentration results from solution-mode ICP-MS (Ag (0.59%) and Au (0.11%)), due to the formation of bigger size Ag_2O (ca. 22 nm)/Au (4.4 nm) particles onto SiO_2.

The catalytic activity of Ag_2O/Au-SiO_2 hybrids

4-Nitrophenol reduction: The reduction of 4-nitrophenol was assessed using $NaBH_4$ and the fabricated catalytic hybrids, to evaluate the catalytic efficiency of harmful pollutant, as it exhibited absorption maxima at 317 nm in distilled water; catalytic reduction of 4-NP was followed by UV–visible absorbance spectroscopy (Fig. 3). The reduction spectra of 4-NP over four hybrids (SBH-Ag/Au-SiO_2, βSBH-Ag/Au-SiO_2, CIT-Ag_2O/Au-SiO_2, and CG-Ag_2O/Au-SiO_2) was tested as a function of reaction time (Supplementary Fig. 4). Using only SiO_2 showed no significant decrease in the 4-nitrophenol absorbance intensity, suggesting a no further reduction in the absence of a catalyst. For the SBH-Ag/Au-SiO_2 and βSBH-Ag/Au-SiO_2 hybrids, under similar conditions, the complete 4-NP reduction was observed in 45 min (Supplementary Fig. 5). This confirmed that there is no significant improvement in the catalytic reduction of 4-NP with β-CD capped SBH-Ag/Au-SiO_2 hybrids. Later, 4-NP reduction was examined for CG-Ag_2O/Au-SiO_2 and CIT-Ag_2O/Au-SiO_2 hybrids which exhibited the complete reduction within 420 and 400 s with a significant increase in the rate of the reaction 0.489 and 0.583 min^{-1} compared to Ag/Au-SiO_2 hybrids, respectively.

In the case of CG-Ag_2O/Au-SiO_2 and CIT-Ag_2O/Au-SiO_2 hybrids, to maintain Ag_2O in the same state, before the introduction of

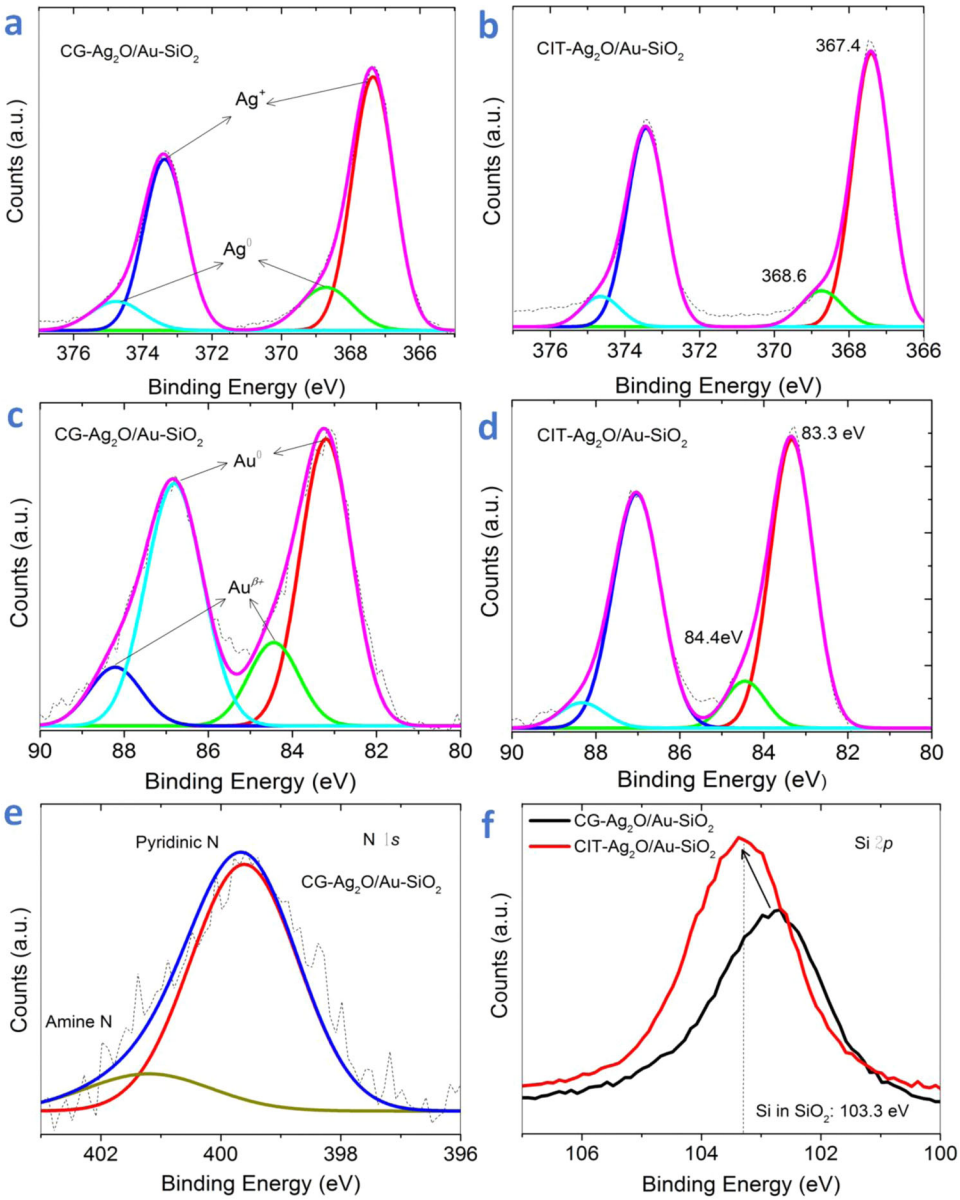

Fig. 3 High-resolution deconvoluted XPS spectra of CG-Ag_2O/Au-SiO_2 and CIT-Ag_2O/Au-SiO_2. High-resolution deconvoluted XPS spectra of **a**, **b** Ag 3*d*, **c**, **d** Au 4*f*, **e** N 1*s* of CG-Ag_2O/Au-SiO_2, and **f** Si 2*p* of both, the CG-Ag_2O/Au-SiO_2 and CIT-Ag_2O/Au-SiO_2.

catalyst, the 4-NP was treated with sufficient $NaBH_4$ to convert it into 4-nitrophenolate ions that were kept for a certain period of time to ensure that all the excess hydrogen has escaped. This step was carried out to keep the state of silver in its Ag^+ state. If $NaBH_4$ was added after adding the catalyst, the strong reducing nature of borohydride ions might reduce the Ag^+ further to Ag^0. So, these catalysts were introduced after forming phenolate ions for efficient conversion while preserving Ag_2O in the same state.

Furthermore, the 4-NP reduction was carried out in the river water spiked samples using CG-Ag_2O/Au-SiO_2 and CIT-Ag_2O/Au-SiO_2 hybrids (Fig. 3b and Supplementary Fig. 4b). Due to the variance in the pH of the aqueous medium, the absorbance maxima of 4-NP exhibited two distinct bands, 317, and 400 nm; the appearance of a new band at 400 nm signifies the formation of the 4-nitrophenolate ion at basic pH (≈7.5). After adding $NaBH_4$ to the above solution, the disappearance of a band at 317 nm was observed, which is similar to distilled water solvent-based reduction reaction. The complete reduction of 4-NP was attained in 300 and 330 s with CG-Ag_2O/Au-SiO_2 or CIT-Ag_2O/Au-SiO_2 hybrids, respectively. The enhancement in the reaction rate was observed in the case of river water samples (i.e., CG-Ag_2O/Au-SiO_2 (0.677 min^{-1}) and CIT-Ag_2O/Au-SiO_2 (0.692 min^{-1})) relative to distilled water samples (Fig. 3d and Supplementary Fig. 4d).

The reduction reaction of 4-NP was further carried out in marine water samples using both CG-Ag_2O/Au-SiO_2 and CIT-Ag_2O/Au-SiO_2 hybrids (Fig. 3c and Supplementary Fig. 4c). As expected, marine water contains many salts that are stable in a basic medium (pH ≈ 9), so the absorbance band for 4-NP completely disappeared at 317 nm and the band appeared at 400 nm attributable to 4-nitrophenolate ion[11]. Interestingly, the complete reduction of 4-NP occurs within 220 and 400 s in the case of CG-Ag_2O/Au-SiO_2 and CIT-Ag_2O/Au-SiO_2 hybrids, respectively. There is a significant decrease in the reaction time, and an enhanced reaction rate (0.911 min^{-1}) was observed in the case of CG-Ag_2O/Au-SiO_2 than CIT-Ag_2O/Au-SiO_2 hybrids in spiked marine water samples (Fig. 3d and Supplementary Fig. 4d), which is possibly due

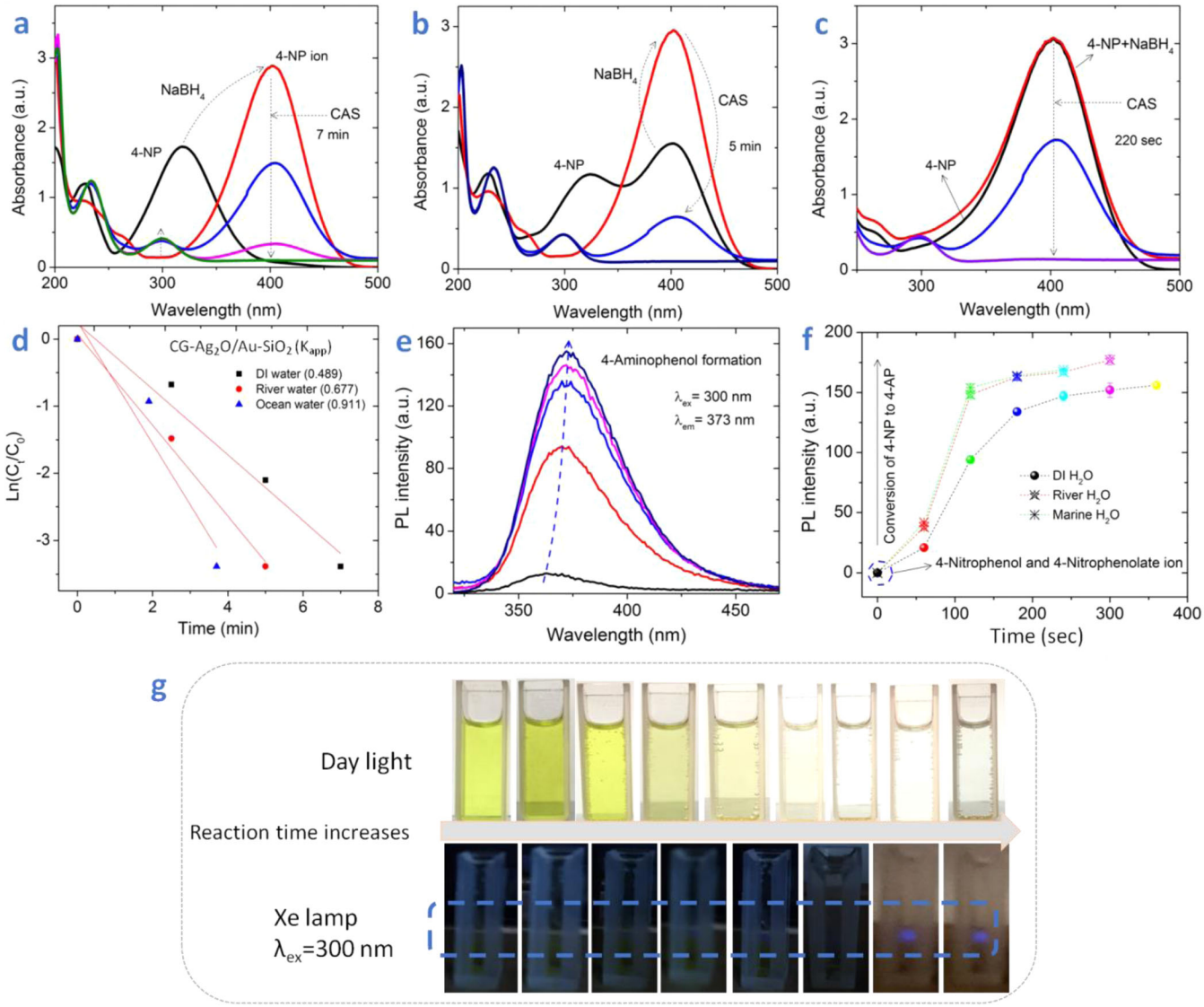

Fig. 4 Time-dependent UV–visible absorbance and photoluminescence spectra of the reduction of 4-nitrophenol, kinetics, and digital photographs. Time-dependent UV–visible absorbance spectra of the catalytic reduction of 4-nitrophenol to 4-aminophenol using CG-Ag_2O/Au-SiO_2 in **a** deionized, **b** river, **c** marine water spiked samples, and the corresponding **d** kinetics of the reaction using pseudo-first-order reaction ($\ln(C_t/C_0 = -kt)$. Time-dependent photoluminescence spectra of the catalytic reduction of 4-nitrophenol to 4-aminophenol using CG-Ag_2O/Au-SiO_2 in **e** deionized water, **f** time vs. PL intensity analysis of deionized, river, and marine water spiked samples, and the corresponding **g** digital photographs under daylight and Xenon lamp (300 nm), respectively.

to the enhancement in the electron transfer from pyridinic N in basic medium.

We also monitored the formation of 4-aminophenol from 4-nitrophenol during the reduction process through an increase in the photoluminescence signal intensity with reaction time at an excitation of 300 nm (Fig. 4e, f), which exhibits the evolution of fluorescence signal at 373 nm attributed from 4-aminophenol. From Fig. 4g, it indicates the formation of 4-aminophenol during the reduction of 4-nitrophenol under 300 nm excitation with xenon lamp.

Methylene blue degradation

The degradation of methylene blue was assessed using $NaBH_4$ and CG-Ag_2O/Au-SiO_2 to evaluate the catalytic efficiency of harmful fluorescent organic basic cationic dye, as it exhibited two absorption maxima at 615 nm (dimer) and 664 nm (monomer) in an aqueous medium; catalytic degradation of MB was followed by real-time UV–visible absorbance and fluorescence spectroscopies[37,40,41]. The degradation spectra of MB over Ag_2O/Au-SiO_2 hybrids were tested as a function of reaction time (Supplementary Fig. 6a, b). Using only SiO_2 and $NaBH_4$ showed no significant decrease in the MB absorbance intensity, suggesting no further reduction in the absence of a catalyst. Under similar conditions, complete degradation was observed in 300, 150, and 60 s for the deionized, river, and marine water spiked samples in presence of CG-Ag_2O/Au-SiO_2 hybrids; faster reduction reaction in the case of marine and river water spiked samples was observed relative to distilled water samples.

Further, methylene blue's similar catalytic degradation activity was monitored by a decrease in the photoluminescence signal intensity with reaction time in the marine, river, and DI water spiked samples at an excitation of 665 nm with an emission signal at 697 nm (Supplementary Fig. 6c, d). The time-dependent digital photographs of MB degradation in marine water samples are presented in Supplementary Fig. 6e, which confirms the efficient

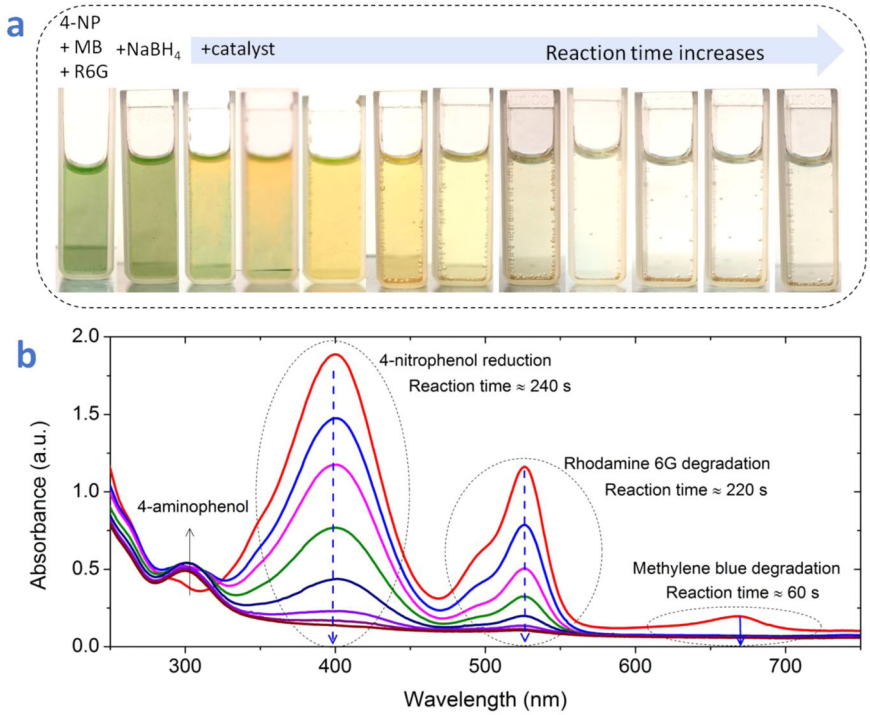

Fig. 5 Digital photographs and time-dependent UV–visible absorbance spectra of the catalytic degradation of mixed organic pollutants. **a** Digital photograph under daylight and the corresponding **b** time-dependent UV–visible absorbance spectra of the catalytic degradation of mixed organic pollutants/dyes (4-nitrophenol, methylene blue, and rhodamine 6G) using CG-Ag_2O/Au-SiO_2 in marine water.

degradation of MB in marine water spiked samples than in the river and deionized water samples.

Rhodamine 6G degradation

Likewise, the degradation of Rhodamine 6G, a harmful fluorescent organic cationic dye, was assessed using $NaBH_4$ and CG-Ag_2O/Au-SiO_2 as it exhibited absorption maxima at 525 nm in deionized water; catalytic degradation of R6G was followed by UV–visible absorbance and fluorescence spectroscopies[37]. The degradation spectra of R6G over Ag_2O/Au-SiO_2 hybrids were tested as a function of reaction time (Supplementary Fig. 7a, b). The deployment of only SiO_2 and $NaBH_4$ showed no significant decrease in the R6G absorbance intensities, suggesting no further reduction in the absence of a catalyst. Under similar conditions, complete degradation was observed in 540, 320, and 300 s in the deionized, river, and marine water spiked samples; again, the decrease in reaction time was observed in the case of the river and marine water samples relative to distilled water samples.

Further, the catalytic degradation of rhodamine 6G was monitored through the decrease in the photoluminescence signal intensity with reaction time at an excitation of 525 nm with an emission signal at 560 nm (Supplementary Fig. 7c, d). The time-dependent visual change under daylight and the xenon lamp digital images were presented in Supplementary Fig. 7e, which confirms the efficient degradation of R6G in marine water visually.

Mixed pollutants degradation

To mimic the contaminated industrial wastewater, the mixed pollutant degradation experiment was carried out[40,42,43]. Similar to the procedure mentioned earlier, the degradation of mixed pollutants (4-NP/MB/Rhodamine 6G) was assessed using $NaBH_4$ and CG-Ag_2O/Au-SiO_2 in marine water samples, and it was monitored by real-time UV–visible absorbance spectroscopy. The degradation spectra of mixed pollutants over Ag_2O/Au-SiO_2 hybrids were assessed as a function of reaction time (Fig. 5). The complete degradation was observed in 240, 220, and 60 s corresponding to 4-NP, MB, and Rhodamine 6G in marine water spiked samples, which confirms the efficiency of the hybrid catalyst to eliminate multiple organic pollutants simultaneously.

Mechanistic insight towards enhanced catalytic efficiencies

Both, the SBH-Ag/Au-SiO_2, and βSBH-Ag/Au-SiO_2 assisted reactions proceed similarly to what has been reported for bare Ag/Au nanoparticles. In brief, the active hydrogen generated upon hydrolysis of $NaBH_4$ will transfer to Ag/Au clusters, which further react with 4-NP ion, MB, and R6G to form respective less toxic products (Supplementary Fig. 8)[41,44]; the rate of reduction is low with the catalysts as mentioned earlier (Table 1). On the other hand, a higher rate of reactions is observed in the case of CG-Ag_2O/Au-SiO_2 and CIT-Ag_2O/Au-SiO_2 hybrids compared to the earlier two catalysts in the present work which may be ascribed to the flow of electrons from Ag_2O to Au clusters and their accumulation on Au due to the formation of ohmic type contact between them thus leading to the accumulation of charges on gold clusters and simultaneously enhancing the reduction process[25]. Among CG-Ag_2O/Au-SiO_2 and CIT-Ag_2O/Au-SiO_2 hybrids, the former, coffee grounds-derived catalyst hybrid, showed higher reduction rates. This enhancement may be attributed to pyridinic N and traces of carbon (from biomass) present in the catalyst; several reports have suggested that the presence of pyridinic N can enhance the catalytic activity with higher rates[29]. The carbon traces also help bring the pollutant and dye molecules closer to the metallic clusters than the catalyst sample without carbon as has been observed by our group previously[45,46]. With these keen reflections, we believe that the formation of an ohmic type contact between Au and Ag_2O and the presence of pyridinic N significantly enhanced the rate of reactions thus explaining the improved performance in catalytic activities by CG-Ag_2O/Au-SiO_2.

Table 1. Comparison of noble metal-based catalysts enabled reduction of 4-NP by $NaBH_4$.

Catalyst (Active catalyst wt%)	Catalyst amount (mg)	C($NaBH_4$)/ C(4-NP)[a]	K_{app} ($\times 10^{-3}$ s^{-1})	K_{app}/M_{ac}[a] (s^{-1} g^{-1}) Existing	K_{app}/M_{as}[a] (s^{-1} g^{-1}) Proposed	Reusable cycles	Ref.
Supported Ag catalyst							
AgNPs (55.2%)/C spheres	1.0	140	1.69	1.69	3.06	NR	[24]
Ag (2.76%)/SiNSs−1	10.0	180	18.05	1.81	65.39	5	[50]
Ag (0.2%)/C	1000	100	5.32	0.005	2.66	10	[19]
Ag (5.40%)/SNTs	5.0	165	38.41	7.68	142.26	5	[27]
CNFs/Ag (61.3%[a])	1.0	40	6.2	6.20	10.12	3	[26]
Fe_3O_4@SiO_2–Ag (NR)	1.0	333	13.6[a]	13.6[a]	–	6	[21]
Ag (10%) @SBA-15	0.9	100	12.74	14.15	141.50	NR	[22]
Ag (8.97%)/KCC-1	0.2	1000	10.00	50.00	558.66	10	[20]
Ag_2 (1.0%)O/Au (1.0%)-DMSNs	0.15	200	13.50	90.00	450	6	[25]
Ag_2O/Au-SiO_2	0.1	200	42.00	420	1120 (XPS), 6000 (ICP-MS)	15	This work
Unsupported Ag catalyst							
AgNCs	4.0	100	5.19	1.30	NA	NR	[23]
Pt@Ag core–shell NPs	0.05	0.1	5.91	118	NA	5	[51]
Ag–Pt Nanowires	0.6	7000	6.93	11.55	NA	NR	[52]
Pt–Ni (96:4)	0.004	150	1.93	482.5	NA	NR	[53]
Au/Ag BMNPs	0.6	7000	6.07	10.1	NA	NR	[54]

NR not reported; *NA* not applicable.
[a]Denoted values were calculated by us.

Proposed activity parameter calculation

Generally, the catalytic activity parameter is calculated using the ratio to the rate of the reaction (K_{app}) and the amount of the catalyst (M_{ac}) (i.e., K_{app}/M_{ac})[25,47]. However, there is a pitfall in this equation as the amount of catalyst will vary on the type of catalyst as has been noticed that the low amount of catalyst used for bare metal nanoparticles (Ag, Au, Pt NPs, and their alloys). In the case of supported catalysts, a higher amount of catalyst is used, in which supports are not participating directly in the catalysis due to a lack of available active sites. Thus, it is always better to use the amount of active catalysts (active sites) in the system. The estimated activity parameter from this study 190, 250, and 420 s^{-1} g^{-1} reduced 4-NP using 30, 100, and 200 mM of $NaBH_4$, which is 4.7 folds higher than the reported Ag_2OAu–DMSNs catalyst (90 s^{-1} g^{-1})[25].

The effect of $NaBH_4$ concentration on the reaction rate and activity parameter was tested using CG-Ag_2O/Au-SiO_2 hybrids in marine water. By increasing the $NaBH_4$ concentration to 100 and 200 mM, the exceptionally improved speed of the reaction was found to be 0.025 and 0.042 s^{-1}, respectively. This response rate suggests that the $NaBH_4$ concentration plays a significant role in the reaction rate, as is apparent from the comparative studies presented in Table 1.

As per the proposed activity parameter calculating method, K_{app}/M_{as} (M_{as} refers to the number of active sites in the catalyst), CG-Ag_2O/Au-SiO_2 hybrids consists of 0.59 (Ag) and 0.11 (Au) wt% (from ICP-MS) of active catalytic sites, the computed activity parameters being 2168, 3571, and 6000 s^{-1} g^{-1} to reduce the 4-NP using 30, 100, and 200 mM of $NaBH_4$ (Table 1).

From the results, the proposed activity parameter values, one should consider the concentration of $NaBH_4$ used for reported catalysts. Therefore, for a better comparison of our results with existing reports, the amount of active catalyst wt% values was considered and presented in Table 1; which established that the CG-Ag_2O/Au-SiO_2 hybrids show the highest activity parameter value of 6000 s^{-1} g^{-1} which was attained with a minimum amount of catalyst. Additionally, the amount of $NaBH_4$ also affects catalytic activity since a higher $NaBH_4$ concentration facilitates the faster 4-NP reduction, and the rate constant value increases.

Zhang et al.[27] have reported Kapp values of 38.41×10^{-3} s^{-1}, and an activity parameter value of 142.26 s^{-1} g^{-1} for the Ag (5.40%)/SNTs comparable K_{app} value but a lower activity parameter compared to CG-Ag_2O/Au-SiO_2 hybrids (42 times higher) due to the usage of higher active catalyst concentration. With the proposed activity parameter calculation, direct and simple comparisons can be easily made for both supported and unsupported Ag catalysts (Table 1).

Catalyst reusability studies

Due to the substantial importance of the stability and reusability of a catalyst for its practical applications, the catalytic stability of the CG-Ag_2O/Au-SiO_2 and CIT-Ag_2O/Au-SiO_2 hybrids was further examined by the recycling 4-NP reduction tests in marine water samples. From Fig. 5, the remarkable catalytic efficiency of the CG-Ag_2O/Au-SiO_2 catalyst was observed with negligible loss (7%) even after 15 reduction cycles of 4-NP (Figs. 6 and 7). In contrast, the CIT-Ag_2O/Au-SiO_2 hybrid catalysts showed a 20% loss in the reduction capacity within 10 cycles (Supplementary Fig. 9) whereas the excellent kinetic reaction rate for CG-Ag_2O/Au-SiO_2 catalyst was maintained at 0.16 ± 0.04 s^{-1} up to 15 cycles (Fig. 7b). Additionally, the XRD pattern of used CG-Ag_2O/Au-SiO_2 exhibited some structural changes (Supplementary Fig. 10). The obtained diffraction patterns at $2\theta \approx 32.0^\circ$, 38.6°, 45.7°, 54.2°, 66.3°, and 75.5° corresponding to Bragg reflections (110), Au (111), (200), (220), (311), and (222), respectively. Interestingly, the lower angle shift in the Ag_2O planes and higher angle shift in the Au (111) plane were observed, which might be due to the expansion and shrinking of interplanar spacing during the catalytic reduction 4-NP. The structural changes in the hybrids further confirm the strong interaction of Ag_2O/Au with the SiO_2 substrate leading to

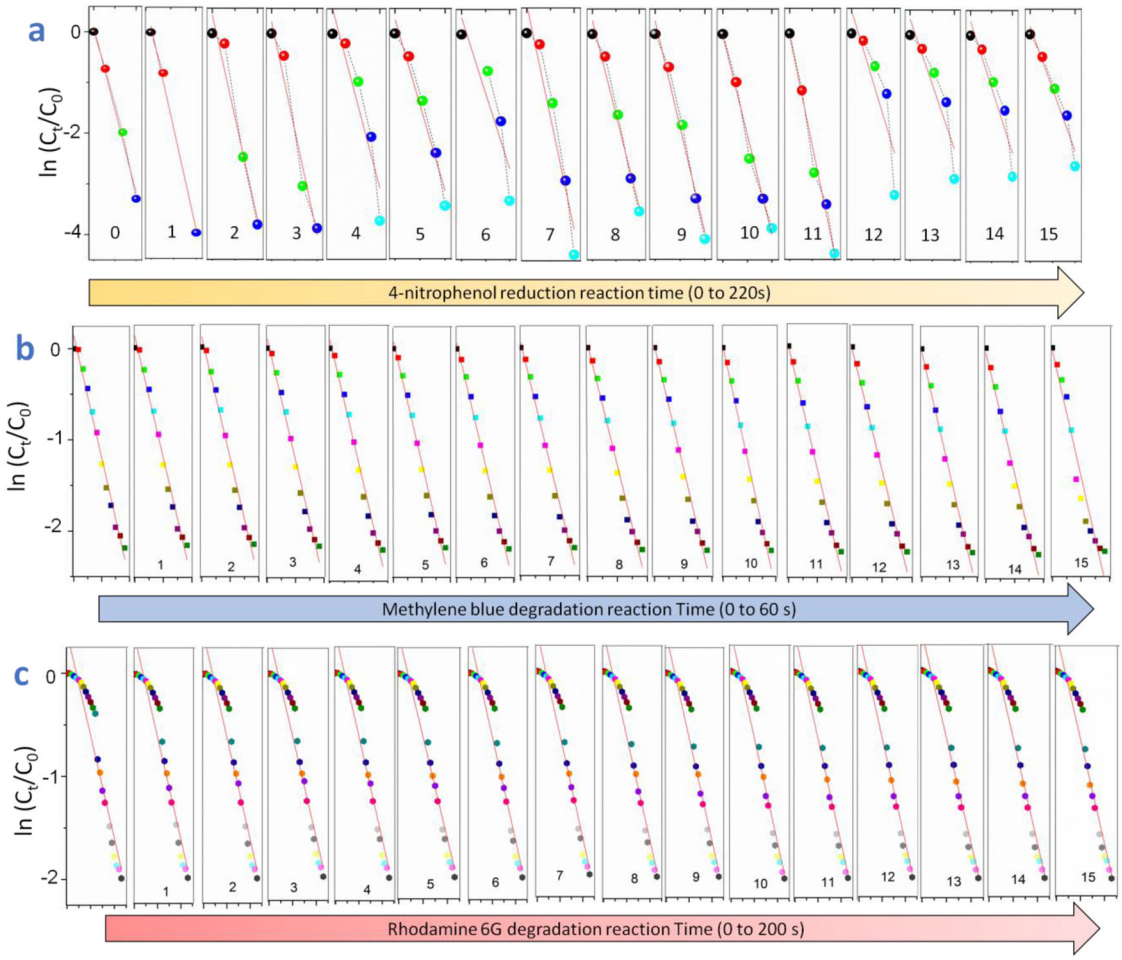

Fig. 6 Pseudo-first-order reaction kinetics for the catalyst reusability for 4-nitrophenol, methylene blue, and rhodamine 6G. Pseudo-first-order reaction kinetics ($\ln (C_t/C_0) = -k_{app}t$) for the catalyst reusability. **a** Reduction of 4-nitrophenol, **b** degradation of methylene blue, and **c** rhodamine 6G using CG-Ag_2O/Au-SiO_2 hybrids up to 15 cycles in marine water samples.

the formation of a stable catalyst for the catalytic reduction reaction (Supplementary Fig. 8). Similar to 4-NP, catalyst reusability in the degradation of MB and rhodamine 6G were studied for up to 15 consecutive cycles using CG-Ag_2O/Au-SiO_2 hybrids; a negligible loss of 2% and 4%, respectively, was discerned in the degradation capacity (Fig. 7a). Whereas the excellent kinetic reaction rate for CG-Ag_2O/Au-SiO_2 catalyst was maintained 0.042 ± 0.02 and $0.019 \pm 0.01\ s^{-1}$ for MB and R6G, respectively, up to 15 cycles (Figs. 6 and 7b).

Theoretical results

The calculations were performed at the density functional theory (DFT) level. A first principal calculation method was used as implemented in Quantum Espresso (QE) package and this package is based on an augmented plane wave (PAW) using pseudopotentials by optimizing valence electronic configuration of Si, O, Ag, N, C, Au, and H was expanded using a set of plane waves with an energy cut-off equal to 520 Ry. The Generalized gradient approximation (GGA) is used to treat the exchange-correlation potential within the functional of Perdew, Burke, and Ernzerhof (PBE). A van der Waals interaction with DFT-D2 Grimme parameterization was applied to correct the long-range interaction, which occurs during the propagation of such wave functions in the simulated materials. For our systems, a self-consistent (SCF) convergence is attained when the energy difference reaches a value smaller than 10^{-6} eV. In contrast, precision for the final forces at all geometrical optimizations must reach a value less than 0.01 eV/Å. A supercell contains 2 x 2 x 1 primitive cells of silica P6/mmm Si4O8 (α-2D-silica) with lattice constants of the cell equal to a1 = a2 = 5.263 Å. A vacuum spacing of 20 Å is chosen to avoid imaginary interactions during the calculation. To identify the Brillouin zone (BZ) integration according to the Monkhorst-Pack mesh, a sampling of 2 x 2 x 1 and 8 x 8 x 1 was used for the optimization and the density of states calculation, respectively. The Au nanocluster, as seen in Fig. 8, is composed of three atoms of Au (Au3). The plasmonic effect is considerable when the number of noble atoms is equal to or higher than three. It could highlight the effectiveness of our model in understanding the experiment. Moreover, to construct the Ag_2O nanocluster, we first built the Ag_2O bulk cleaved in (110) direction to construct the surface. In next step was building a supercell. From the such surface, we cut atoms from all directions to obtain the small geometry nanostructure of Ag_2O. Then, the final geometry of this nanocluster was found after performing an optimization calculation. As a result, the obtained Ag_2O nanocluster comprises six atoms of Ag and four atoms of O, as depicted in Fig. 8. Optimizing the 4-NP is also performed using the same DFT framework. We calculated the adsorption energy of 4-NP on our substrates using the following expression: DE_{ads} = E(substrate+4-NP) - E(substrate)-E(4-NP)In which E(substrate+4-NP) is the energy of the 4-NP adsorbed on the substrate, E (substrate) is the energy of different substrates, and E(4-NP) is the energy of the 4-NP in an isolated state. The charge density difference was determined using the

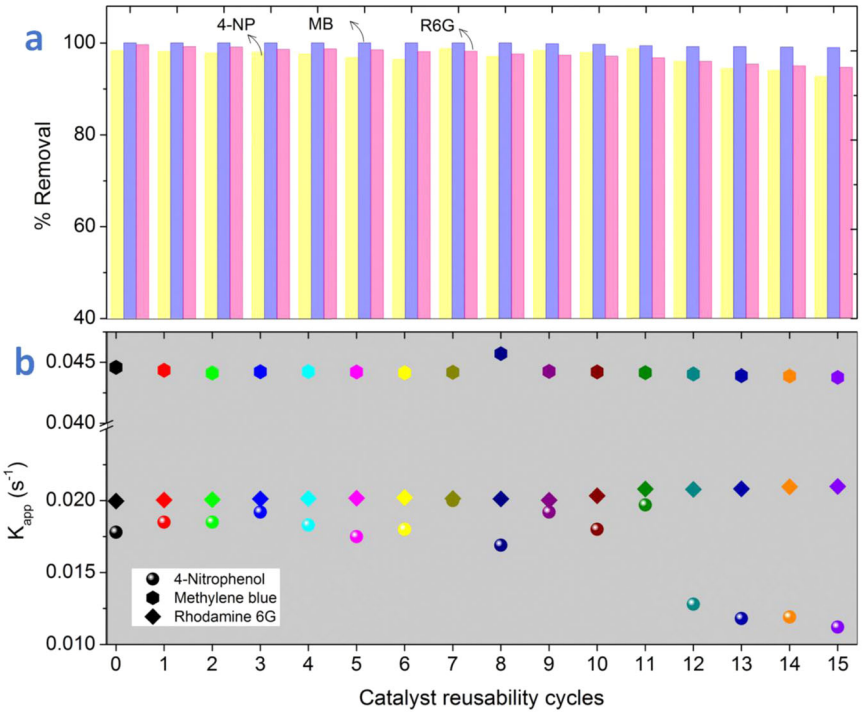

Fig. 7 Re-usability cycles vs. % removal and rate constant, for the reduction of 4-nitrophenol, methylene blue, and rhodamine 6G. Re-usability up to 15 cycles vs. **a** % removal and **b** rate constant (Kapp (s^{-1})), for the reduction of 4-nitrophenol and degradation of methylene blue and rhodamine 6G using CG-Ag_2O/Au-SiO_2 hybrids catalyst in marine water spiked samples.

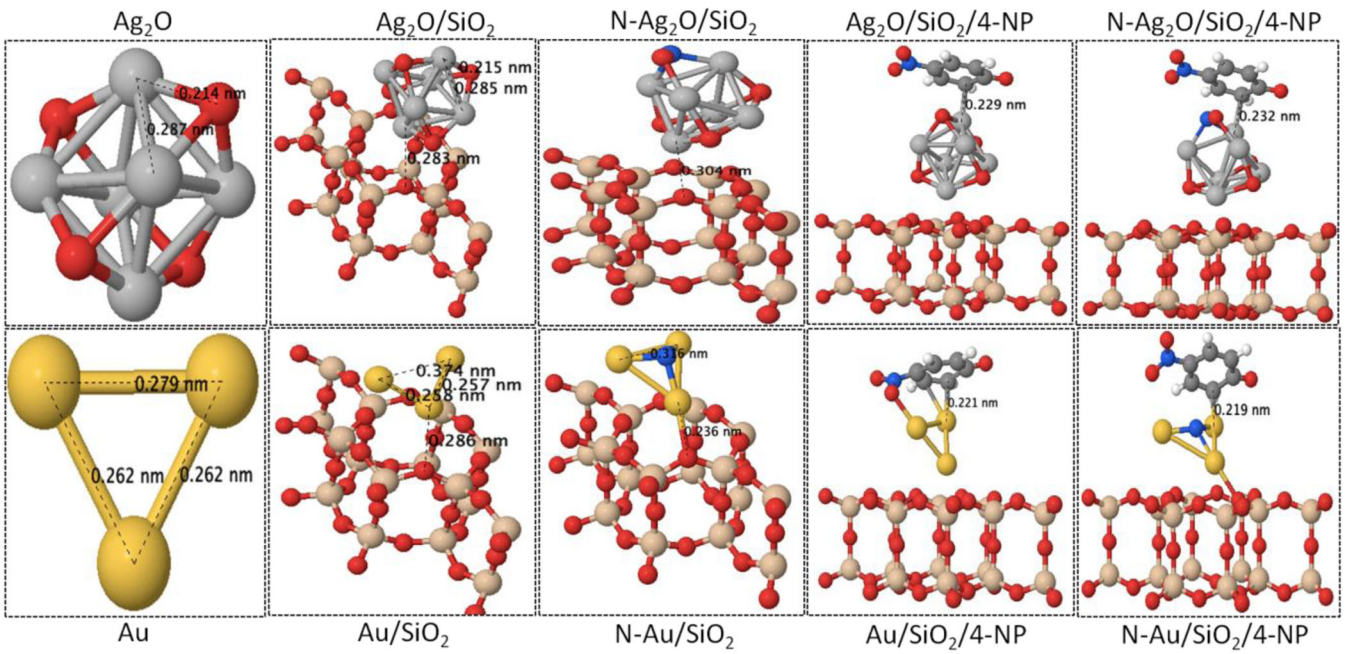

Fig. 8 DFT studies for the catalytic systems optimized. DFT studies for the catalytic systems Ag_2O (upper row) and Au (bottom row) optimized, bare systems (Ag_2O and Au), silica-supported systems (Ag_2O/SiO_2, Au/SiO_2, N-Ag_2O/SiO_2, N-Au/SiO_2) and with the presence of 4-nitrophenol onto supported systems (Ag_2O/SiO_2/4-NP, Au/SiO_2/4-NP, N-Ag_2O/SiO_2/4-NP, N-Au/SiO_2/4-NP).

same DFT methodology. The charge transfer analysis of the 4-NP on substrates with and without the addition of N was analyzed using Bader analysis. The isosurfaces of electronic density differences were mapped and determined with the following equation: Dr = r(substrate+4-NP) - r(substrate)- r(4-NP), in which r(substrate+4-NP) is the charge of 4-NP/substrate systems; r(substrate) is the charge of the substrates, and r(4-NP) is the charge density of the isolated 4-NP. In this case, also the 4-NP is adsorbed on SiO_2-Au, SiO_2-Au+N, SiO_2-Ag_2O, and SiO_2-Ag_2O+N substrates. The bond lengths of Au/SiO_2 and N-Au/SiO_2 between Au and O on SiO_2 were found to be 0.286 and 0.236 nm, respectively (Fig. 8). This confirms that the presence of N makes the Au more stable and adsorbed onto the SiO_2 system by forming a strong bond. Moreover, the adsorption energy for Au/

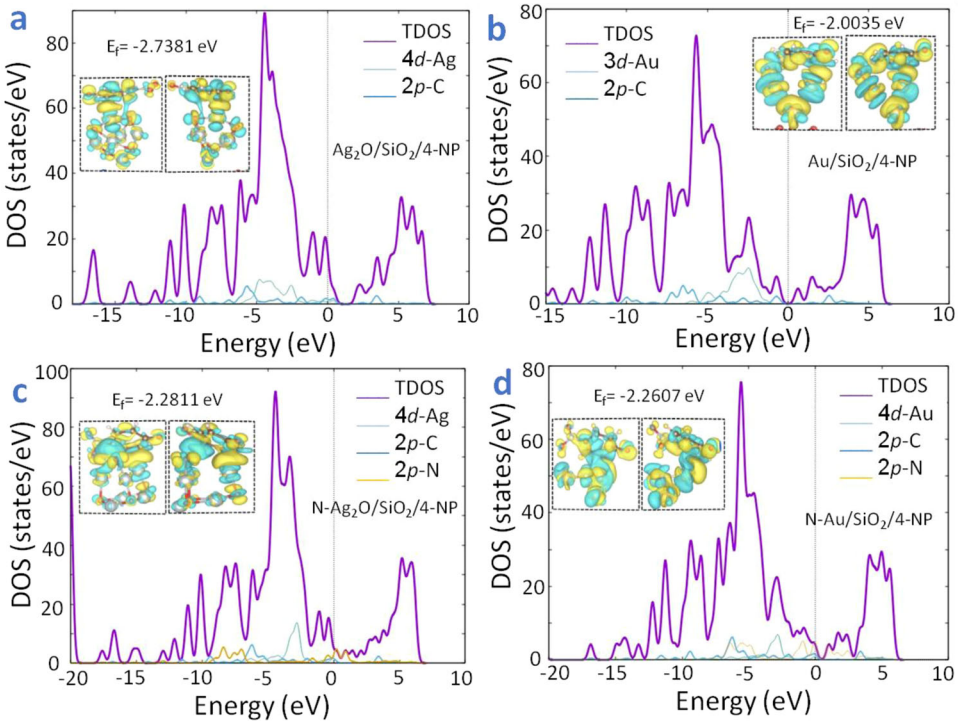

Fig. 9 TDOS results of the catalytic systems with 4-nitrophenol. TDOS results of the catalytic systems with 4-nitrophenol: **a** Ag_2O/SiO_2/4-NP, **b** N-Ag_2O/SiO_2/4-NP, **c** Au/SiO_2/4-NP, and **d** N-Au/SiO_2/4-NP.

SiO_2 being negative (−2.72 eV), substantiating that the optimized systems are thermodynamically stable. However, for Ag_2O/SiO_2 and N-Ag_2O/SiO_2 systems, there is a weak bonding interaction existing between the two components (O (of SiO_2) and Ag (of Ag_2O)) with a distance value of 0.283 and 0.304 nm for Ag_2O/SiO_2 and N-Ag_2O/SiO_2, respectively. It is worth noting that the adsorption energy of the Ag_2O/SiO_2 system is also negative (−0.96 eV), reinforcing that the Au/ SiO_2 system is more stable than Ag_2O/SiO_2 system.

Further, we calculated the adsorption energies for Au/SiO_2, Ag_2O/SiO_2, N-Au/SiO_2, and N-Ag_2O/SiO_2 in the presence of 4-NP which were found to be −3.34, −1.05, −17.43, and −18.21 eV, respectively[48,49]. Interestingly, higher adsorption energy values were observed in the case of N-anchored catalytic systems than other catalysts presented in this work. The bond lengths between Au/Ag and C of the benzene ring of 4-NP are 0.221 and 0.229 nm for Au/SiO_2 and Ag_2O/SiO_2 systems, respectively. These values affirm the formation of strong bonding between the metals (Au and Ag) with the 4-NP molecule. In the case of N-anchored systems, the distance is higher than (N-Au/SiO_2 (0.219 nm) and N-Ag_2O/SiO_2 (0.232 nm)) those without N systems and noticed a slight difference in the rotation between the basal plane of the initially 4-NP deposited and the optimized one[48,49].

In addition, the charge transfer analysis was performed with a net charge of 0.431|e| for Au/SiO_2 and 0.122|e| for Ag_2O/SiO_2 in 4-NP which confirms the significant adsorption of the Au than the Ag_2O system. A similar tendency of charge transference followed in the case of N-Au/SiO_2 (0.320|e|) and N-Ag_2O/SiO_2 (0.136|e|). Apparently, the catalyst system needs a highly polarized area in the presence of the support that should stabilize the clusters to permit the transition of the electrons from the conduction band (CB) of the metals to the CB of the 4-NP; a partial charge analysis of all four catalysts was performed.

In the case of N-Au/SiO_2/4-NP (10.658|e| (Au) and 5.665|e| (N)), the charge transfer was more toward the N atom than toward the 4-NP molecule. While the case of Au/SiO_2/4-NP (10.827|e|(Au)) observed higher charge transfer than N-Au/SiO_2/4-NP. This authenticates that the Au/SiO_2 system with highly polarized Au and high transference of electrons toward 4- NP is responsible for the effective degradation of 4-NP[48,49].

Similarly, the charge transfer analysis was performed for Ag_2O/SiO_2 and N-Ag_2O/SiO_2. From the obtained results, N-Ag_2O/SiO_2 (10.495|e| (Ag)) exhibited better charge transfer than Ag_2O/SiO_2 (10.309|e| (Ag)), and N has a net charge equal to 4.943|e| in the case of N-Ag_2O/SiO_2. The Ag in N-Ag_2O/SiO_2 has more charge in its shell due to the N that aid in the injection of electrons with a high concentration to the CB of the material to 4-NP.

We performed total and partial density of states for four systems as mentioned earlier. As presented in Fig. 9, a small bandgap exists for all systems except N-Ag_2O/SiO_2 thus affirming the metallic behavior of N-Ag_2O/SiO_2. This means that all systems present different conductivity, and the materials that present a small bandgap preferably would have a better conductivity compared to the pristine SiO_2. As a result, the electrons could jump quickly from the VB to the CB composed of Au-3*d* and Ag-4*d* to the CB of the 4-NP for easy removal of the 4-NP. However, in the case of Ag_2O/SiO_2, we noted occupation states of the 4*d*-Ag band at lower energies.

In contrast, 4*d*-Ag in N-Ag_2O/SiO_2 presents a better overlapping with the 2*p*-C atoms, and the higher states of the electronic occupation of the same orbital are near the Fermi level. The 2*p* N atoms transfer electrons to the nearest 4*d*-Ag states; these electronic transfers polarize the region between the metal and the C atoms to degrade the molecule. For this reason, we observed that 2*p*-electrons are non-filled occupied states (yellow color line located above the Fermi level). In the case of N-Au/SiO_2/4-NP and Au/SiO_2/4-NP systems, the occupation of the 3*d* of Au without N is higher than that of N, and the N atoms attracted more electrons. For this reason, we observed filled states for 2*p*-N, which lower the covalence between the C-2*p* and 3*d*-Au.

Meanwhile, in the case of Au/SiO_2/4-NP, the system tends to stabilize 3*d*-Au orbitals near the Fermi level, which means higher occupancy of electrons than in the other cases. Still, the conductivity in this system is lower due to the larger bandgap

presented. It could be a retarding effect of the transition of the hot electrons to the CB for molecular degradation. For this reason, we conclude that for our materials, the addition of an N atom would improve the degradation of the 4-NP compared to the case without the N atoms (Supplementary Table 1).

In this work, we have successfully fabricated the Ag/Au-SiO_2 and Ag_2O/Au-SiO_2 using four different reducing catalysts via a simple in situ synthesis protocol. The presence of pyridinic nitrogen in green-fabricated Ag_2O/Au-SiO_2 effectively enhances the interfacial Au and N electron transfer. Further, it exhibited superior catalytic efficiency relative to chemically fabricated Ag_2O/Au in marine water samples. The reusability assessments of CG-Ag_2O/Au-SiO_2 up to 15 cycles without much loss confirmed the remarkable stability of the fabricated catalyst. Notably, the CG-Ag_2O/Au-SiO_2 catalyst displays the highest activity parameter for Ag NPs reported to date to reduce 4-nitrophenol, methylene blue, and rhodamine 6G in marine water. The importance of pyridinic N in the Ag_2O and Au is also scrutinized through first-principles calculations, which are performed to model the studied systems. The free energies, adsorption energies, charge transfer, and density of states calculations confirm the predominant role of N in Ag_2O-based systems for superior catalytic activity. As the doping with heteroatom's changes the electronic structure and enhances the amount of charge at the adsorbent–adsorbate interface, DFT validates the tendency toward enhanced catalytic efficiencies via a N-Ag_2O and Au NPs surface. More importantly, the present fabrication strategy offers an innovative opportunity for synthesizing other similar metal and metal oxide nanoparticle hybrids for varied applications.

METHODS

Materials

In this work, *Equisetum myriohaetum* (Mexican Giant Horsetail) was obtained from Morelos state, Mexico, and the coffee grounds used were left over from *Coffea arabica* seed powder that was purchased from the local supermarket, in Oaxaca state, Mexico. Gold chloride solution ($HAuCl_4$, 99.9% trace metals basis, 30 wt% in dilute HCl), silver nitrate ($AgNO_3$, ACS reagent ≥99.0%), sodium borohydride ($NaBH_4$, 99.99%), β-cyclodextrin (β-CD, ≥97.0%), sodium citrate (CIT, US pharmacopeia standard), 4-nitrophenol (4-NP, spectrophotometric grade), Methylene blue (MB, ≥95%), Rhodamine 6G (R6G, 99%), concentrated hydrochloric acid (37%, HCl), (3-aminopropyl) triethoxysilane (APTES), ammonium hydroxide (28%) were obtained from Sigma Aldrich-Mexico utilized as received. River and seawater were secured from Morelos state and Acapulco Sea basin, respectively.

Synthesis of biogenic porous SiO_2 from *Equisetum myriohaetum*

The biogenic silica was extracted from *Equisetum myriohaetum* (Mexican Giant Horsetail) as described earlier[8]. In brief, the stems of the plant (*Equisetum myriohaetum)* were separated and oven-dried at 50 °C before acid digestion in concentrated HNO_3/H_2SO_4 (4:1), where 25 g of dried starting material was processed with 1 L of acid. The mixture was stirred and left in a fume hood until a white precipitate was obtained and the release of nitrogen oxides ceased (usually around 48 h). The residue was then separated and washed with copious amounts of deionized water until the pH value of the supernatant reached about 5. The sample was then lyophilized before heat treatment in the air at 650 °C for 5 h, at the heating rate of 10 °C/min.

Fabrication of amine-functionalized SiO_2 substrates

The amine-functionalized biogenic silica is obtained using 3-aminopropyl) triethoxysilane (APTES)[8]. Typically, 10.0 mL of APTES and 1.0 g of silica were added to 0.1 L of ethanol. The mixture was stirred at room temperature for 8 h. The ensued APTES-modified 3D silica substrates were separated by centrifugation at 6500 rpm, washed several times with ethanol and water, and then re-dispersed in 100 mL of distilled water.

Used coffee grounds powder extract preparation

The 8 g L^{-1} of the sun-dried used coffee grounds (CG) powder, obtained from a solution of CA seed powder (10 g L^{-1}), was taken in a glass beaker with distilled water and kept at a temperature (i.e., 75 ± 5 °C) for 30 min. Further, the used coffee grounds powder (CG) extract was cooled to ambient temperature and centrifuged and filtered using a Wattman filter paper.

Fabrication of Ag/Au ions decorated SiO_2 hybrid structures

About 1:1 volumetric ratio of an $AgNO_3$ solution (3 mM) and $HAuCl_4$ (1 mM) was added to 1.0 g of amine-functionalized SiO_2 substrates under agitation. After 8 h, the visual color of the reaction solution turned from white to pale yellow. Next, the samples were separated from the reaction mixture by centrifugation at 6000 rpm to remove excess metal ions and then re-dispersed in 10 mL of DI water.

Fabrication of hybrid structures

About 40 mL of freshly prepared CG extract solution was added to Ag and Au ions decorated SiO_2 particles under agitation at 60 ± 5 °C. Within 5 min, the visual color of the solution turned from pale yellow to dark brown, which is indicative of the formation Ag_2O/Au-SiO_2 hybrid catalysts. Lastly, the Ag_2O/Au-SiO_2 hybrids were separated by centrifugation at 7000 rpm for 30 min. A similar procedure was followed for fabricating sodium citrate-mediated Ag_2O/Au-SiO_2 hybrids (0.4 g of CIT) and was named CIT-Ag_2O/Au-SiO_2 hybrids. Further, freshly prepared $NaBH_4$ (0.1 g) was added to Ag and Au ions decorated SiO_2 particles at room temperature to secure SBH-Ag/Au-SiO_2 hybrids. To fabricate βSBH-Ag/Au-SiO_2 hybrids, 0.1 g of β-CD was mixed with SBH-Ag/Au-SiO_2 hybrids and kept overnight under agitation.

Characterization

X-ray diffraction (XRD) analysis of the powder samples was carried out using a Bruker D8 Advance eco diffractometer, using CuKα ($\lambda = 1.5406$ Å) radiation. The size, morphology, and composition of the hybrid catalysts were studied using High-resolution transmission electron microscopy (HR-TEM) images acquired using a JEOL JEM 2200Fs+Cs (aberration corrector). X-ray photoelectron spectroscopy (XPS) was recorded on an ESCA Ulvac-PHI 1600 photoelectron spectrometer from Physical Electronics using Al Kα radiation photon energy of 1486.6 ± 0.2 eV. The dual-beam Perkin-Elmer Lambda 950 spectrophotometer was utilized for monitoring the reduction of 4-NP by the hybrid catalysts. The Cary eclipse fluorescence spectrophotometer was utilized for real-time monitoring of the catalytic experiments using CG-Ag_2O/Au-SiO_2. The ICP-MS analysis was performed by the plasma source mass spectrometry method with model iCAP Qc-Thermo Scientific instrument which was optimized prior to the analysis of the samples, with a certified aqueous solution of the High Purity Standards brand (SM-1595-143), comprising a wide range of masses (Li, Co, In, Ba, Bi, Ce and U of 1 µg/L, respectively). The calibration curve was made with 15 points (0, 0.1, 0.25, 0.5, 0.75, 1, 2.5, 5, 7.5, 10, 25, 50, 75, 100 and 250 µg/L), from stock solution multi-elemental of Au, Ir, Os, Pd, Pt, Rh, Ru, and Ag (ICP-MS-68A-Solution C) of 10 mg/L.

Catalytic experiments

The 4-nitrophenol reduction experiments were carried out with 0.1 mg of each hybrid catalyst, i.e., SBH-Ag/Au-SiO_2, βSBH-Ag/Au-SiO_2, CG-Ag_2O/Au-SiO_2, and CIT-Ag_2O/Au-SiO_2. The measured amount of hybrid catalyst (0.1 mg) was mixed with 0.5 mL of aqueous 4-NP (1.0 mM) to form a mixture solution. Subsequently, 0.5 mL of a freshly prepared $NaBH_4$ solution (30 mM) was added to the earlier mixture is distilled, river, and marine water samples. The time-dependent catalytic degradation process was monitored using UV–visible absorbance and photoluminescence spectroscopies. A similar procedure was followed for the degradation of individual MB, R6G, and 4-NP/MB/R6G mixture using CG-Ag_2O/Au-SiO_2. All the experiments in this work were performed under ambient conditions and in triplicate.

Reusability studies

The procedure stated above was used to investigate the reusability of the fabricated hybrid catalysts as the recovered catalysts were collected after the complete elimination of 4-NP, MB, and R6G in marine water samples. The reclaimed catalysts were washed repeatedly using DI water followed by centrifugation. The amount of catalyst, concentration, and volume of 4-NP/MB/R6G and $NaBH_4$ solutions used for the recyclability tests were mainlined the same; catalytic tests were performed at room temperature without stirring the reaction mixture.

DATA AVAILABILITY

The data that support the findings of this study are available from the corresponding author upon reasonable request.

CODE AVAILABILITY

Code available from the corresponding author upon reasonable request.

Received: 17 December 2021; Accepted: 22 August 2022;
Published online: 08 September 2022

REFERENCES

1. Cheng, H. et al. Recyclable Ag/halloysite nanotubes/polyvinyl alcohol sponges for enhanced reduction of 4-nitrophenol. *Appl. Clay Sci.* **223**, 106510 (2022).
2. Keshri, K. S. & Chowdhury, B. Effect of the Ag–CeO_2 interaction and the nature of pore structure on the catalytic activities of different Ag–CeO_2/mesoporous-SiO_2 catalysts on the reduction of 4-nitrophenol. *J. Porous Mater.* **29**(3), 893–906 (2022).
3. Long, L. et al. 3D printing of recombinant *Escherichia coli*/Au nanocomposites as agitating paddles towards robust catalytic reduction of 4-nitrophenol. *J. Hazard. Mater.* **423**, 126983 (2022).
4. Mahaulpatha, B. H. et al. Catalytic reduction of 4-nitrophenol using CuO@ $Na_2Ti(PO_4)_2{\cdot}H_2O$. *J. Environ. Sci. Health Part A* **57**(1), 65–79 (2022).
5. Zhuang, J. et al. In-situ growth of heterophase Ni nanocrystals on graphene for enhanced catalytic reduction of 4-nitrophenol. *Nano Res.* **15**(2), 1230–1237 (2022).
6. Fu, J. et al. A dual-response ratiometric fluorescence imprinted sensor based on metal-organic frameworks for ultrasensitive visual detection of 4-nitrophenol in environments. *Biosens. Bioelectron.* **198**, 113848 (2022).
7. Yuan, H., Yu, J., Feng, S. & Gong, Y. Highly photoluminescent pH-independent nitrogen-doped carbon dots for sensitive and selective sensing of *p*-nitrophenol. *RSC Adv.* **6**, 15192–15200 (2016).
8. Bogireddy, N. K. R. et al. Platinum nanoparticle-assembled porous biogenic silica 3D hybrid structures with outstanding 4-nitrophenol degradation performance. *Chem. Eng. J.* **388**, 124237 (2020).
9. Islam, M. T., Sultana, K. A. & Noveron, J. C. Borohydride-free catalytic reduction of organic pollutants by platinum nanoparticles supported on cellulose fibers. *J. Mol. Liq.* **296**, 111988 (2019).
10. Wang, Y. et al. One-pot green synthesis of bimetallic hollow PdPt nanotubes for enhanced catalytic reduction of *p*-nitrophenol. *J. Colloid Interface Sci.* **539**, 161–167 (2019).
11. Petrenko, I. et al. Extreme biomimetics: preservation of molecular detail in centimeter-scale samples of biological meshes laid down by sponges. *Sci. Adv.* **5**, 1–12 (2019).
12. Yao, Y. et al. Synthesis and characterization of iron–nitrogen-doped biochar catalysts for organic pollutant removal and hexavalent chromium reduction. *J. Colloid Interface Sci.* **610**, 334–346 (2022).
13. Sun, Q., Han, B., Li, K., Yu, L. & Dong, L. The synergetic degradation of organic pollutants and removal of Cr (VI) in a multifunctional dual-chamber photocatalytic fuel cell with Ag@ Fe_2O_3 cathode. *Sep. Purif. Technol.* **281**, 119966 (2022).
14. Fu, Y. et al. Recent progress of noble metals with tailored features in catalytic oxidation for organic pollutants degradation. *J. Hazard. Mater.* **422**, 126950 (2022).
15. Wang, M., Dai, S., Gan, N. & Wang, Y. In situ growth of silver nanoparticles on polydopamine-coated chalcogenide glass tapered fiber for the highly sensitive detection of volatile organic compounds in water. *J. Non-Cryst. Solids* **581**, 121420 (2022).
16. Ali, M. E., Abouelfadl, M., Badway, N. A. & Salam, K. M. Effective removal of organic compounds using a novel cellulose acetate coated by PA/g-CN/Ag nanocomposite membranes. *Surf. Interfaces* **29**, 101748 (2022).
17. Benmaati, A. et al. Insights into catalytic reduction of organic pollutants catalyzed by nanoparticles supported on zeolite clinoptilolite. *Silicon* **14**, 1–13 (2022).
18. Hosny, M. et al. Facile synthesis of gold nanoparticles for anticancer, antioxidant applications, and photocatalytic degradation of toxic organic pollutants. *ACS Omega* **7**(3), 3121–3133 (2022).
19. Chi, Y., Tu, J., Wang, M., Li, X. & Zhao, Z. One-pot synthesis of ordered mesoporous silver nanoparticle/carbon composites for catalytic reduction of 4-nitrophenol. *J. Colloid Interface Sci.* **423**, 54–59 (2014).
20. Dong, Z. et al. Silver nanoparticles immobilized on fibrous nano-silica as highly efficient and recyclable heterogeneous catalyst for reduction of 4-nitrophenol and 2-nitroaniline. *Appl. Catal. B Environ.* **158–159**, 129–135 (2014).
21. Ge, J., Zhang, Q., Zhang, T. & Yin, Y. Core-satellite nanocomposite catalysts protected by a porous silica shell: controllable reactivity, high stability, and magnetic recyclability. *Angew. Chem.* **120**, 9056–9060 (2008).
22. Naik, B., Hazra, S., Prasad, V. S. & Ghosh, N. N. Synthesis of Ag nanoparticles within the pores of SBA-15: an efficient catalyst for reduction of 4-nitrophenol. *Catal. Commun.* **12**, 1104–1108 (2011).
23. Rashid, M. H. & Mandal, T. K. Synthesis and catalytic application of nanostructured silver dendrites. *J. Phys. Chem. C* **111**, 16750–16760 (2007).
24. Tang, S., Vongehr, S. & Meng, X. Carbon spheres with controllable silver nanoparticle doping. *J. Phys. Chem. C* **114**, 977–982 (2010).
25. Yang, T. Q. et al. Interfacial electron transfer promotes photo-catalytic reduction of 4-nitrophenol by Au/Ag2O nanoparticles confined in dendritic mesoporous silica nanospheres. *Catal. Sci. Technol.* **9**, 5786–5792 (2019).
26. Zhang, P. et al. In situ assembly of well-dispersed Ag nanoparticles (AgNPs) on electrospun carbon nanofibers (CNFs) for catalytic reduction of 4-nitrophenol. *Nanoscale* **3**, 3357–3363 (2011).
27. Zhang, Z. et al. Tubular nanocomposite catalysts based on size-controlled and highly dispersed silver nanoparticles assembled on electrospun silica nanotubes for catalytic reduction of 4-nitrophenol. *J. Mater. Chem.* **22**, 1387–1395 (2012).
28. Qing, L. et al. Selectively nitrogen-doped carbon materials as superior metal-free catalysts for oxygen reduction. *Nat. comm.* **9**, 3376 (2018).
29. Ortiz-Medina, J. et al. Catalytic nanocarbons: defect engineering and surface functionalization of nanocarbons for metal-free catalysis. *Adv. Mater.* **31**, 1970096 (2019).
30. Yuxian, W. et al. Mechanistic investigations of the pyridinic N−Co structures in Co embedded N-doped carbon nanotubes for catalytic ozonation. *ACS EST Eng.* **1**, 32–45 (2021).
31. Jing, H. et al. Functionalization of covalent organic frameworks by metal modification: construction, properties and applications. *Chem. Eng. J.* **404**, 127136 (2021).
32. Hong, M. et al. Polymer brush-assisted preparation of magnetic Au nanocatalyst for highly efficient reduction of organic pollutants. *Colloids Surf. A: Physicochem. Eng. Asp.* **639**, 128338 (2022).
33. Misra, M., Chattopadhyay, S., Sachan, A. & Sachan, S. G. Microbially synthesized nanoparticles and their applications in environmental clean-up. *Environ. Technol. Rev.* **11**(1), 18–32 (2022).
34. Zhu, Y. et al. Silver nanoparticles-decorated and mesoporous silica coated single-walled carbon nanotubes with an enhanced antibacterial activity for killing drug-resistant bacteria. *Nano Res.* **13**, 389–400 (2020).
35. Yang, Y. et al. Silica-coated silver nanoparticles decorated with fluorescent CdTe quantum dots and DNA aptamers for detection of tetracycline. *ACS Appl. Nano Mater.* **3**, 9796–9803 (2020).
36. Fan, H. T. et al. Ordered mesoporous silica cubic particles decorated with silver nanoparticles: a highly active and recyclable heterogeneous catalyst for the reduction of 4-nitrophenol. *Dalton Trans.* **48**, 2692–2700 (2019).

37. Lu, Z., Giles, L. W., Teo, B. M. & Tabor, R. F. Carbon dots as a 'green'reagent to produce shape and size controlled gold nanoparticles for application in pollutant degradation. *Colloid Inteface Sci. Commun.* **46**, 100571 (2022).
38. Laouini, S. E. et al. Green synthesized of Ag/Ag_2O nanoparticles using aqueous leaves extracts of *Phoenix dactylifera* L. and their azo dye photodegradation. *Membranes* **11**, 468 (2021).
39. Margaret, J. M. Ascorbic acid content of some miscellaneous tropical and subtropical plants and plant products. *J. Food Sci.* **17**, 31–35 (1952).
40. Bogireddy, N. K. R. et al. Green fabrication of 2D platinum superstructures and their high catalytic activity for mitigation of organic pollutants. *Catal. Today* **360**, 185–193 (2021).
41. Eltaweil, A. S. et al. Green synthesis of platinum nanoparticles using *Atriplex halimus* leaves for potential antimicrobial, antioxidant, and catalytic applications. *Arab. J. Chem.* **15**(1), 103517 (2022).
42. Fatemeh, A., Mahmoud, N. & Mahsa, M. Self-assembled lignosulfonate-inorganic hybrid nanoflowers and their application in catalytic reduction of methylene blue and 4-nitrophenol. *Sep. Purif. Technol.* **272**, 118864 (2021).
43. Min, Z. et al. Promotion effects of halloysite nanotubes on catalytic activity of Co3O4 nanoparticles toward reduction of 4-nitrophenol and organic dyes. *J. Hazard. Mater.* **403**, 123870 (2021).
44. Zhao, P., Feng, F., Huang, D., Yang, G. & Astruc, D. Basic concepts and recent advances in nitrophenol reduction by gold- and other transition metal nanoparticles. *Cord. Chem. Rev.* **287**, 114–136 (2015).
45. Kesarla, M. K. et al. Transformation of $g\text{-}C_3N_4$ into onion like carbon on nickel nanoparticles for ultrafast hydrogenation. *Mater. Chem. Phy.* **240**, 122157 (2020).
46. Bogireddy, N. K. R. et al. Integration of nitrogen-doped graphene oxide dots with Au nanoparticles for enhanced electrocatalytic hydrogen evolution. *ACS Appl. Nano Mater.* **4**(11), 11513–11525 (2021).
47. Varshney, S., Bar-Ziv, R. & Zidki, T. On the remarkable performance of silver-based alloy nanoparticles in 4-nitrophenol catalytic reduction. *ChemCatChem* **12**, 4680–4688 (2020).
48. Santana, E. et al. Adsorption study of 4-nitrophenol onto kaolinite (001) surface: a van der Waals density functional study. *Mater. Chem. Phys.* **271**, 124887 (2021).
49. Tianran, L. et al. A silk-like hydrogen-bonded organic framework functionalized membrane with intrinsic catalytic activity for nonmetallic reduction of 4-nitrophenol. *Chem. Eng. J.* **441**, 136092 (2022).
50. Yan, Z., Fu, L., Zuo, X. & Yang, H. Green assembly of stable and uniform silver nanoparticles on 2D silica nanosheets for catalytic reduction of 4-nitrophenol. *Appl. Catal. B Environ.* **226**, 23–30 (2018).
51. Lv, Z. S. et al. One-pot synthesis of highly branched Pt@Ag core-shell nanoparticles as a recyclable catalyst with dramatically boosting the catalytic performance for 4-nitrophenol reduction. *J. Colloid Interface Sci.* **538**, 349–356 (2019).
52. Wang, Y., Wang, X., Sun, B., Tang, S. & Meng, X. Concentration-dependent morphology control of Pt-coated-Ag nanowires and effects of bimetallic interfaces on catalytic activity. *J. Mater. Sci. Technol.* **32**, 41–47 (2016).
53. Ghosh, S. K., Mandal, M., Kundu, S., Nath, S. & Pal, T. Bimetallic Pt–Ni nanoparticles can catalyze reduction of aromatic nitro compounds by sodium borohydride in aqueous solution. *Appl. Catal. A Gen.* **268**, 61–66 (2004).
54. Huang, J. et al. Ag dendrite-based Au/Ag bimetallic nanostructures with strongly enhanced catalytic activity. *Langmuir* **25**, 11890–11896 (2009).

ACKNOWLEDGEMENTS

N.K.R.B. acknowledge Dirección General de Asuntos del Personal Académico (DGAPA) de la UNAM for postdoctoral fellowship. We express special gratitude to Ma. Cristina Zorrilla Cangas and Antonio Morales Espino, Institute of Physics-UNAM for UV–vis, TEM, and XRD analysis. The authors thank Ma. C. Elizabeth Hernández Alvarez for her analytical support in determining the trace elements by ICP-MS, Institute of Geophysics, UNAM.

AUTHOR CONTRIBUTIONS

N.K.R.B.: Conceptualization; data curation; formal analysis; investigation; methodology; project administration; validation; visualization; roles/writing—original draft. A.G.E.H.: Data curation; formal analysis; roles/writing—original draft. Y.R.M.: Writing—original draft; formal analysis. M.K.K.: Formal analysis; writing—original draft. R.H.B.: Resources; supervision; project administration. R.S.V.: Data curation; writing—review & editing. V.A.: Conceptualization; formal analysis; resources; software; supervision; project administration; validation; visualization; writing—review & editing.

COMPETING INTERESTS

The authors declare no competing interests.

ADDITIONAL INFORMATION

Supplementary information The online version contains supplementary material available at https://doi.org/10.1038/s41545-022-00187-w.

Correspondence and requests for materials should be addressed to Naveen Kumar Reddy Bogireddy or Vivechana Agarwal.

Reprints and permission information is available at http://www.nature.com/reprints

Publisher's note Springer Nature remains neutral with regard to jurisdictional claims in published maps and institutional affiliations.